

Mid-ocean-ridge seismicity reveals extreme types of ocean lithosphere

Vera Schlindwein¹ & Florian Schmid¹

Along ultraslow-spreading ridges, where oceanic tectonic plates drift very slowly apart, conductive cooling is thought to limit mantle melting¹ and melt production has been inferred to be highly discontinuous^{2–4}. Along such spreading centres, long ridge sections without any igneous crust alternate with magmatic sections that host massive volcanoes capable of strong earthquakes⁵. Hence melt supply, lithospheric composition and tectonic structure seem to vary considerably along the axis of the slowest-spreading ridges⁶. However, owing to the lack of seismic data, the lithospheric structure of ultraslow ridges is poorly constrained. Here we describe the structure and accretion modes of two end-member types of oceanic lithosphere using a detailed seismicity survey along 390 kilometres of ultraslow-spreading ridge axis. We observe that amagmatic sections lack shallow seismicity in the upper 15 kilometres of the lithosphere, but unusually contain earthquakes down to depths of 35 kilometres. This observation implies a cold, thick lithosphere, with an upper aseismic zone that probably reflects substantial serpentinization. We find that regions of magmatic lithosphere thin dramatically under volcanic centres, and infer that the resulting topography of the lithosphere–asthenosphere boundary could allow along-axis melt flow, explaining the uneven crustal production at ultraslow-spreading ridges. The seismicity data indicate that alteration in ocean lithosphere may reach far deeper than previously thought, with important implications towards seafloor deformation and fluid circulation.

Mid-ocean ridges continuously produce new ocean lithosphere that consists of a layer of ocean crust (on average 6–8 km thick) underlain by mantle lithosphere⁷. The upper part of the mantle lithosphere is mechanically strong and brittle to temperatures of 650 ± 100 °C (ref. 8) and is referred to here as elastic lithosphere. The base of the oceanic lithosphere is defined by an isotherm of 1,000–1,300 °C (ref. 9). Once the spreading rate drops below about 20 mm yr^{-1} conductive cooling reduces melt production and a different class of mid-ocean ridge forms that produces anomalous ocean lithosphere in 10%–20% of the world's oceans². Geological exploration of the poorly accessible ultraslow spreading ridges in the Arctic Ocean and the Southwest Indian Ocean revealed up to 100-km-long rift sections with mantle rocks exposed at the sea floor^{2–4}, indicating little mantle melt production. Between these sections pronounced volcanic centres receive more melt than the regional average and show an over-thickened crust³. Further observations that clearly distinguish ultraslow-spreading ridges from other mid-ocean ridges are the unexpectedly high incidence rate of hydrothermal plumes relative to the low magma budget¹⁰, a particular, smooth seafloor morphology⁶ and the potential to produce moment magnitude $M > 6$ earthquakes⁵. However, the lithospheric structure of ultraslow-spreading ridges is little known. Classic terms that describe the ocean lithosphere, such as 'crust' and 'Moho', lose their meaning in the absence of magmatism¹¹. Active-source seismic imaging of this anomalous lithosphere has been conducted only recently at the most accessible parts of ultraslow-spreading ridges and is unable to characterize lithospheric structure beyond its shallowest domains¹².

Records of local seismicity have greatly advanced our understanding of active spreading processes, the lithospheric structure and the thermal regime of most spreading ridges¹³ but no such data exist for ultraslow-spreading ridges. Following a 10-day feasibility study near Logachev Seamount on Knipovich Ridge¹⁴ (Fig. 1, site 2), we undertook the first concerted effort to compare the seismicity of contrasting magmatic and amagmatic sections of ultraslow spreading ridges. We recorded local earthquakes on one of the most extensive amagmatic sections of ultraslow spreading ridges, the oblique supersegment on the Southwest Indian Ridge (SWIR) (Fig. 1, site 1), with eight ocean bottom seismometers (OBSs) for a period of 11 months in 2012–2013 (ref. 15). The data set is unique because the long-term deployment of OBSs in the stormy Furious Fifties (the area between 50° S and 60° S, which is prone to strong winds), where only few research vessels can operate, has not been attempted before. A similar OBS network was installed simultaneously at a magmatic section, the Segment-8 volcanic centre on the eastern SWIR (Fig. 1, site 3) where an episode of teleseismic earthquake swarms occurred between 1996 and 2003 (ref. 5).

We determined the hypocentre locations of all of the recorded microearthquakes (see Methods). Figure 1 and Extended Data Figs 1–3 show a distinct image of hypocentre depths along 390 km of ultraslow-spreading ridges representing the prevalent background seismicity at local magnitudes of $M_l = 0.5$ –3. The unprecedented clarity and consistency of the seismicity throughout the three representative sections allows us to state three key observations that expand previous knowledge of mid-ocean-ridge seismicity with important inferences for lithospheric structure.

(1) Earthquakes reach maximum depths of 35 km below the sea floor in areas with peridotite exposure, surpassing by far the deepest known mid-ocean-ridge earthquakes at about 15 km depth¹⁶.

(2) The clear lower boundary of seismicity, which provides constraints on the thickness of the axial elastic lithosphere (see Methods), varies dramatically along-axis, thinning by up to 15 km under volcanoes or sites of basalt exposure.

(3) Regions in the upper lithosphere are entirely aseismic. They occur mainly in peridotite-dominated ridge sections and extend to 15 km depth (Fig. 1; site 1, 40–75 km along the profile).

Melt flow along an undulating permeability boundary near the lithosphere–asthenosphere boundary towards magmatic centres is a key hypothesis in ultraslow ridge research that has been put forward by several authors^{17–19} to account for the pronounced variations in the crustal thickness, seafloor rock composition and tectonic structure observed along ultraslow spreading ridges. Our data show that the base of the elastic lithosphere as imaged by maximum hypocentre depths varies dramatically along-axis, being shallowest under volcanic centres (Fig. 1). If we assume that the permeability boundary near the lithosphere–asthenosphere boundary displays the same topography (see Methods) we can estimate the along-axis extent of the catchment areas where melts can flow upslope towards magmatic centres. These areas are at least 60–120 km in length and are hence consistent with the typical

¹Alfred Wegener Institute, Helmholtz Centre for Polar and Marine Research, Am Alten Hafen 26, 27568 Bremerhaven, Germany.

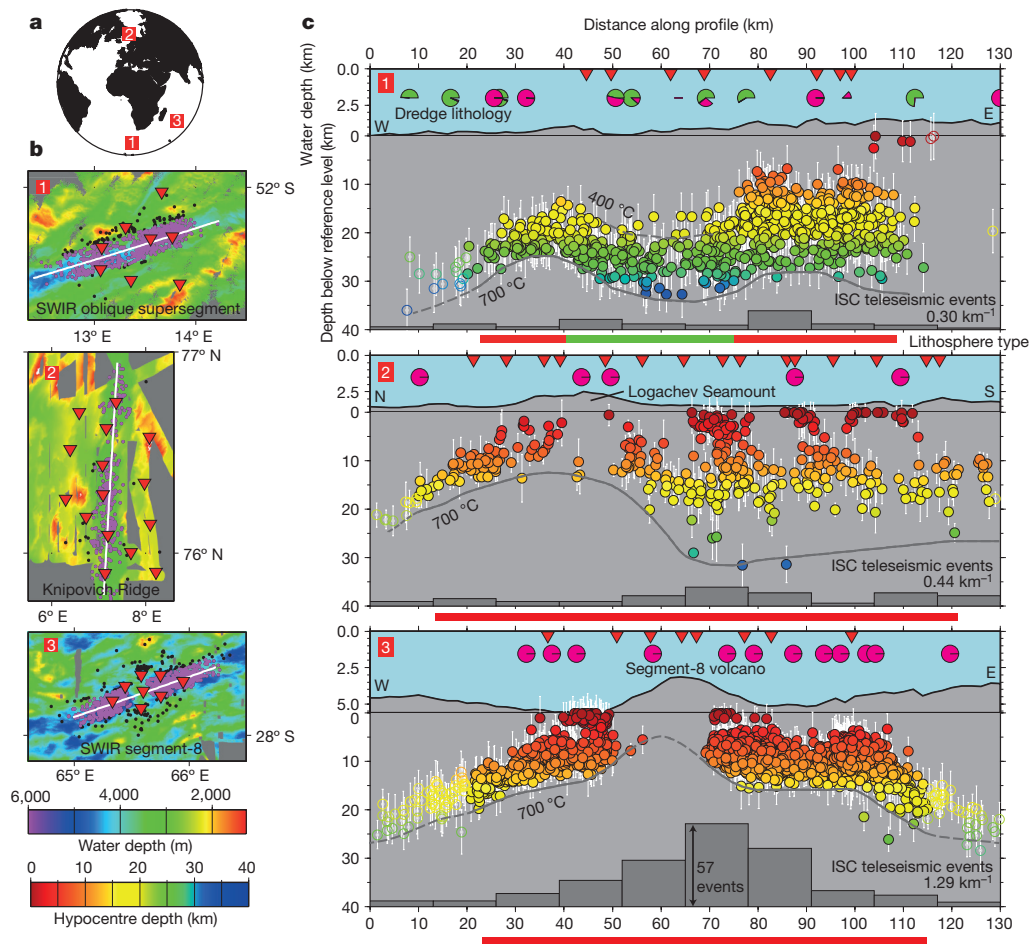


Figure 1 | Along-axis seismicity of ultraslow-spreading ridges. **a**, Study sites 1–3 on Knipovich Ridge and the SWIR. **b**, Maps of the study areas. White lines indicate the positions of transects in **c**. Red triangles are the OBS positions. Black dots mark earthquake locations, magenta dots are earthquakes that are projected onto the transects in **c**. All high-resolution bathymetry data are from RV *Polarstern* except SWIR segment-8 (ref. 6). **c**, Along-axis hypocentre depths (indicated by the colour coding, open circles are for those beyond the network) with error bars showing the 95% confidence level. The temperature regime is indicated by the estimated isotherms (grey lines, dashed where uncertain). The grey histograms indicate the numbers of teleseismic earthquakes from the Reviewed Bulletin of the International Seismological Centre (ISC; <http://www.isc.ac.uk/iscbulletin/search/bulletin/#reviewed>) along the ridge axis⁵ with the average event rates per kilometre of the rift axis labelled. The bathymetry is exaggerated vertically by a factor of 2.5 above the reference level (defined by the deepest OBS) marked by a thin horizontal line. The dredge lithology is shown in the pie charts (site 1 data from ref. 2, data for sites 2 and 3 are from <http://www.earthchem.org/petdb>): green, peridotite; magenta, basalt. The lithosphere type (green for amagmatic, red for magmatic) is indicated underneath the profiles where the OBS network provides sufficient constraint.

segment lengths of ultraslow-spreading ridges of about 100 km^{17,20}. Our data thus provide geophysical support for the hypothesis of melt focusing over segment-scale distances.

Peridotite may alter to mechanically weak phyllosilicates such as serpentinite (lizardite) in fractures that are penetrated by seawater up to temperatures of about 400 °C (refs 21 and 22). Volume fractions of only 10% serpentinite can drastically reduce the strength of the lithosphere and may lead to strain localization in distinct aseismic shear zones²³. We propose that the extensive aseismic regions, observed in peridotite-dominated, amagmatic ridge sections (Fig. 1; site 1, 40–75 km along the profile), result from serpentinization of the upper lithosphere either along distinct, deep-reaching shear zones that concentrate strain or through pervasive alteration of at least 10% of the mantle rocks. In this interpretation, the observed low seismic velocities at these depth levels (Extended Data Fig. 1b) reflect partial serpentinization²³. The onset of seismicity, and hence of brittle faulting below, occurs at a depth where temperatures of roughly 400 °C (for the estimate see Methods) are reached and serpentinite becomes unstable. The upper limit of seismicity in amagmatic regions may therefore image the serpentinization front at previously unknown depths of up to 15 km. This implies in turn that fluid circulation extends to these depths to alter the mantle rocks, exploiting major shear zones or a network of microfractures²⁴.

The adjacent magmatic regions, however, exhibit brittle deformation at depths of 8–15 km in the upper mantle or even throughout the lithosphere (Fig. 1; site 1, 75–115 km along the profile, site 2). Serpentinization in these mantle domains is apparently less

pronounced and cannot effectively reduce the shear strength, so these regions of the mantle behave more like normal ocean lithosphere, where serpentinization is commonly confined to the uppermost mantle^{23,24}. We therefore speculate that differences in lithospheric composition favour serpentinization of the upper mantle in amagmatic lithosphere but limit serpentinization of magmatic lithosphere at the same depth levels. Alternatively, there may be differences in the connectivity of the fluid pathways that enable or prevent deeply penetrating water circulation in amagmatic and magmatic lithosphere, respectively.

To assess the relevance of our local seismicity surveys we examined the teleseismic earthquake record of ultraslow-spreading ridges⁵. The average numbers of earthquakes per kilometre of rift axis (for calculation see Methods) confirm the different deformation styles of predominantly magmatic and amagmatic rift segments (Figs 1 and 2 and Extended Data Fig. 4). Figure 2 and Extended Data Fig. 4 illustrate these differences for Gakkel Ridge and the SWIR, respectively: more abundant, stronger and often clustered earthquakes coincide with basalt exposure and a strong central magnetic anomaly in the magmatic Western Volcanic Zone, whereas reduced seismicity correlates with the occurrence of peridotite and an absence of magnetic anomalies in the Sparsely Magmatic Zone. Earthquakes there tend to be connected to minor basalt exposures. Volcanic centres may host extensive teleseismic earthquake swarms despite their locally thin elastic lithosphere (Fig. 1, site 3). The repeated teleseismic earthquake swarms between 1996 and 2003 at the Segment-8 volcano potentially mark a phase of magmatic activity⁵. The complete absence of seismicity underneath the volcano

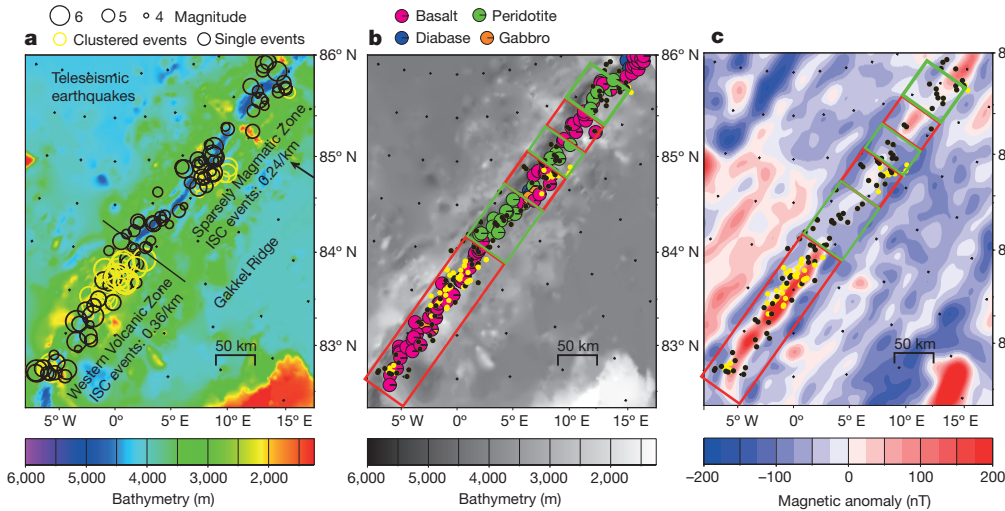


Figure 2 | Contrasting magmatic and amagmatic sections of Gakkel Ridge. **a**, Teleseismic earthquake activity (open circles, scaled with magnitude) over the bathymetry. Yellow circles mark earthquake clusters of two or more events related in time and space. Off-axis highs (arrow) extending away from the ridge axis indicate the long-term stability of this segmentation pattern. Teleseismic event rates are also indicated for comparison between sections. **b**, Dredge lithology. Data from ref. 4. **c**, Magnetic anomalies. Data from ref. 31. Earthquakes from **a** are shown by the dots. Magmatic lithosphere (red boxes) shows more and stronger earthquakes, basalt exposure and magnetic anomalies. Amagmatic lithosphere (green boxes) shows less seismicity, peridotite exposure and lacks a central magnetic anomaly.

during our survey in 2012–2013 may therefore be a result of increased temperatures caused by recent magmatism.

From the teleseismic and local seismicity records, we can thus define two end-member types of ocean lithosphere representative for ultraslow-spreading ridges (Figs 1–3). The first type, ‘amagmatic lithosphere’, has an elastic thickness of up to 35 km and lacks an igneous crust. Its serpentinized mantle rocks carry only weak magnetization²⁵ and are prone to deep-reaching serpentinization that results in aseismic deformation in the upper part of the lithosphere. Amagmatic lithosphere therefore shows a prominent reduction in seismicity. The second type, ‘magmatic lithosphere’, is thinner and shallows towards volcanoes. A thin, igneous crust carrying a remanent magnetization is present²⁵. Magmatic lithosphere is stronger, with considerable seismicity throughout its elastic portion. As it has experienced some melting and melt migration, we speculate that a different lithospheric composition may prevent extensive serpentinization. Dredge statistics from Gakkel Ridge and the SWIR show a higher percentage of gabbroic veins in magmatic lithosphere than in amagmatic lithosphere²⁶, potentially suggesting that more melts are being trapped at shallower levels in magmatic lithosphere (Fig. 3). However, as both extensive alteration to large depths and trapped melts could account for the observed low seismic velocities in our one-dimensional velocity models of the lithospheric mantle (Extended Data Figs 1b, 2b and 3b), our data can highlight only the different deformation styles of magmatic and amagmatic lithosphere, not determine their petrologic cause. Future high-resolution seismic studies combined with geological sampling are needed to determine the detailed velocity structure and composition of the end-member types of lithosphere described here.

However, the recognition of these lithosphere types and their geophysical characteristics leads to a conceptual advance in the understanding of ultraslow lithosphere accretion, which we sketch in Fig. 3 for Gakkel Ridge. The extensive circulation of water through amagmatic lithosphere may further cool and thicken the lithosphere locally, leading to a pronounced topography of its base that enables along-axis flow of melt on the segment scale towards the topographic shoals under magmatic zones. These magmatic zones vary in size from tiny patches in amagmatic zones (Fig. 1; site 1, 35 km and 90 km along the profile, see also the Sparsely Magmatic Zone in Figs 2 and 3), to volcanic centres with different thermal and magmatic states (Fig. 1, sites 2 and 3, and the Eastern Volcanic Zone in Fig. 3) and to robustly magmatic zones with extended along-axis magmatism (the Western Volcanic Zone in Figs 2 and 3). Lithospheric thinning is observed in all cases but the vertical amount and the lateral extent vary. The complete lack of seismicity at volcanic centres observed in our short survey period may indicate high temperatures connected to recent magmatic activity; it is likely to be transient given the observed teleseismic earthquake activity in these areas over longer periods. The variable appearance of magmatic lithosphere may therefore be caused by differences in lithospheric thickness, together with differences in the geometry and effectiveness of melt extraction²⁶, and by differences in melt availability, which is dependent on the mantle composition and fertility³. In addition to spatial variability, melt delivery is also expected to vary in time at a given location. As seismicity provides only snapshots in time of the lithospheric structure, the variable appearance of magmatic lithosphere also reflects different stages in its temporal evolution.

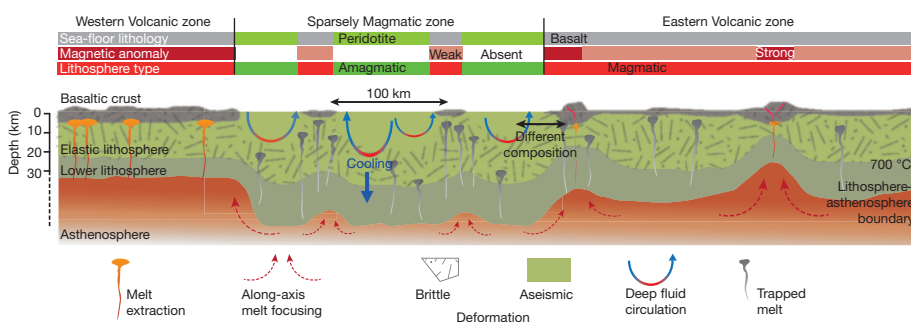


Figure 3 | Conceptual sketch of the two lithosphere types at the Gakkel Ridge. Scales are approximate. Deep-reaching alteration in amagmatic ridge sections cools and further thickens the lithosphere. The pronounced topography of the lithosphere–asthenosphere boundary focuses melts towards magmatic sections. Melt ascent there may result in a different lithospheric composition that is less prone to alteration and demonstrates brittle behaviour, whereas amagmatic lithosphere can deform aseismically.

We show that lithospheric thinning in magmatic sections is not the only factor that produces a topography of the lithosphere–asthenosphere boundary. The proposed deep-reaching serpentinization of amagmatic lithosphere implies extensive water circulation that in turn results in the cooling of the lithosphere from above. Spatially variable cooling of the lithosphere may therefore also contribute to enhancing the topography of the lithosphere–asthenosphere boundary. Once this topography is established, the process is self-sustaining. Gakkel Ridge, Knipovich Ridge and the western SWIR show off-axis highs that extend away from volcanic centres in the spreading direction and a spatially stable seafloor magnetic anomaly pattern (Fig. 2), both of which document long-term stability of the lithospheric accretion modes. Any reorganization of this pattern as observed on the eastern SWIR requires large instabilities such as a rapid cooling and thickening of the lithosphere at magmatic centres to prevent further melt pooling¹⁷.

Our study provides geophysical constraints on the along-axis thermal structure of ultraslow spreading ridges, against which a multitude of petrologic models of ultraslow spreading^{18,26,27} can be validated. A further insight is that ultraslow spreading ocean lithosphere exhibits a completely different deformation mode that we attribute to alteration of mantle rocks reaching 15 km depth.

This deformation style distinguishes ultraslow-spreading ridges from faster-spreading ridges: slow-spreading ridges show a dominant pattern of higher levels of seismicity at the colder, magma-poor segment ends¹³, in contrast to what we observe at the ultraslow-spreading ridges where less seismicity is associated with amagmatic regions. Exhumation of mantle lithosphere along major detachment faults produces substantial earthquake activity at the Mid-Atlantic Ridge^{13,28}. The seismicity delineates the detachment faults to depths of 7 km into the shallow upper mantle²⁹. At ultraslow-spreading ridges, detachment faulting is also thought to be a fundamental process in mantle rock exhumation³⁰ and the generation of smooth sea floor⁶, but our study suggests that deformation along such shear zones occurs entirely aseismically owing to deep-reaching serpentinization, explaining the contrasting seismicity pattern of slow- and ultraslow-spreading ridges.

Serpentinization in young oceanic lithosphere is generally believed to be limited to shallow depths of 4–6 km below detachment faults, but its extent is generally difficult to estimate from seismic velocities or rock samples gained from dredging or drilling²⁴. Our data suggest that in the extensive amagmatic regions of ultraslow-spreading ridges serpentinization and fluid circulation may reach far deeper into the mantle than previously assumed.

Online Content Methods, along with any additional Extended Data display items and Source Data, are available in the online version of the paper; references unique to these sections appear only in the online paper.

Received 22 October 2015; accepted 18 April 2016.

Published online 29 June 2016.

- Bown, J. W. & White, R. S. Variation with spreading rate of oceanic crustal thickness and geochemistry. *Earth Planet. Sci. Lett.* **121**, 435–449 (1994).
- Dick, H., Lin, J. & Schouten, H. An ultraslow-spreading class of ocean ridge. *Nature* **426**, 405–412 (2003).
- Sauter, D. & Cannat, M. The ultraslow spreading Southwest Indian Ridge. *Geophys. Monogr. Ser.* **188**, 153–173 (2010).
- Michael, P. J. *et al.* Magmatic and amagmatic seafloor generation at the ultraslow-spreading Gakkel ridge, Arctic Ocean. *Nature* **423**, 956–961 (2003).
- Schindwein, V. Teleseismic earthquake swarms at ultraslow spreading ridges: indicator for dyke intrusions? *Geophys. J. Int.* **190**, 442–456 (2012).
- Cannat, M. *et al.* Modes of seafloor generation at a melt-poor ultraslow-spreading ridge. *Geology* **34**, 605–608 (2006).
- White, R. S., McKenzie, D. & O'Nions, R. K. Oceanic crustal thickness from seismic measurements and rare earth element inversions. *J. Geophys. Res.* **97**, 19683–19715 (1992).
- Anderson, D. L. Lithosphere, asthenosphere, and perisphere. *Rev. Geophys.* **33**, 125–149 (1995).

- Cannat, M. How thick is the magmatic crust at slow spreading oceanic ridges? *J. Geophys. Res.* **101**, 2847–2857 (1996).
- Edmonds, H. N. *et al.* Discovery of abundant hydrothermal venting on the ultraslow-spreading Gakkel Ridge in the Arctic Ocean. *Nature* **421**, 252–256 (2003).
- Cannat, M. Emplacement of mantle rocks in the seafloor at mid-ocean ridges. *J. Geophys. Res.* **98**, 4163–4172 (1993).
- Niu, X. *et al.* Along-axis variation in crustal thickness at the ultraslow spreading Southwest Indian Ridge (50°E) from a wide-angle seismic experiment. *Geochem. Geophys. Geosyst.* **16**, 468–485 (2015).
- Escartin, J. *et al.* Central role of detachment faults in accretion of slow-spreading oceanic lithosphere. *Nature* **455**, 790–794 (2008).
- Schindwein, V., Demuth, A., Geissler, W. H. & Jokat, W. Seismic gap beneath Logachev Seamount: indicator for melt focusing at an ultraslow mid-ocean ridge? *Geophys. Res. Lett.* **40**, 1703–1707 (2013).
- Schindwein, V. The expedition of the research vessel “Polarstern” to the Antarctic in 2013 (ANT-XXIX/8). *Rep. Polar Marine Res.* **672**, 14–22 (2014).
- Dusunur, D. *et al.* Seismological constraints on the thermal structure along the Lucky Strike segment (Mid-Atlantic Ridge) and interaction of tectonic and magmatic processes around the magma chamber. *Mar. Geophys. Res.* **30**, 105–120 (2009).
- Cannat, M., Rommevaux-Jestin, C. & Fujimoto, H. Melt supply variations to a magma-poor ultra-slow spreading ridge (Southwest Indian Ridge 61° to 69°E). *Geochem. Geophys. Geosyst.* **4**, 9104 (2003).
- Montési, L. G. J., Behn, M. D., Hebert, L. B., Lin, J. & Barry, J. L. Controls on melt migration and extraction at the ultraslow Southwest Indian Ridge 10°–16°E. *J. Geophys. Res.* **116**, B10102 (2011).
- Standish, J. J., Dick, H. J. B., Michael, P. J., Melson, W. G. & O'Hearn, T. MORB generation beneath the ultraslow spreading Southwest Indian Ridge (9–25°E): major element chemistry and the importance of process versus source. *Geochem. Geophys. Geosyst.* **9**, Q05004 (2008).
- Cannat, M., Rommevaux-Jestin, C., Sauter, D., Deplus, C. & Mendel, V. Formation of the axial relief at the very slow spreading Southwest Indian Ridge (49° to 69°E). *J. Geophys. Res.* **104**, 22825–22843 (1999).
- Amiguet, E. *et al.* Creep of phyllosilicates at the onset of plate tectonics. *Earth Planet. Sci. Lett.* **345–348**, 142–150 (2012).
- Schwartz, S. *et al.* Pressure–temperature estimates of the lizardite/antigorite transition in high pressure serpentinites. *Lithos* **178**, 197–210 (2013).
- Escartin, J., Hirth, G. & Evans, B. Strength of slightly serpentinized peridotites: implications for the tectonics of oceanic lithosphere. *Geology* **29**, 1023–1026 (2001).
- Rouméjon, S. & Cannat, M. Serpentinization of mantle-derived peridotites at mid-ocean ridges: mesh texture development in the context of tectonic exhumation. *Geochem. Geophys. Geosyst.* **15**, 2354–2379 (2014).
- Sauter, D., Cannat, M. & Mendel, V. Magnetization of 0–26.5 Ma seafloor at the ultraslow spreading Southwest Indian Ridge, 61°–67°E. *Geochem. Geophys. Geosyst.* **9**, Q04023 (2008).
- Sleep, N. H. & Warren, J. M. Effect of latent heat of freezing on crustal generation at low spreading rates. *Geochem. Geophys. Geosyst.* **15**, 3161–3174 (2014).
- Cannat, M. *et al.* Spreading rate, spreading obliquity, and melt supply at the ultraslow spreading Southwest Indian Ridge. *Geochem. Geophys. Geosyst.* **9**, Q04002 (2008).
- Simão, N. *et al.* Regional seismicity of the Mid-Atlantic Ridge: observations from autonomous hydrophone arrays. *Geophys. J. Int.* **183**, 1559–1578 (2010).
- deMartin, B. J., Sohn, R. A., Pablo Canales, J. & Humphris, S. E. Kinematics and geometry of active detachment faulting beneath the Trans-Atlantic Geotraverse (TAG) hydrothermal field on the Mid-Atlantic Ridge. *Geology* **35**, 711–714 (2007).
- Sauter, D. *et al.* Continuous exhumation of mantle-derived rocks at the Southwest Indian Ridge for 11 million years. *Nat. Geosci.* **6**, 314–320 (2013).
- Maus, S. *et al.* EMAG2: a 2-arc min resolution Earth Magnetic Anomaly Grid compiled from satellite, airborne, and marine magnetic measurements. *Geochem. Geophys. Geosyst.* **10**, Q08005 (2009).

Acknowledgements This study was enabled by grants SCHL853/1-1 and SCHL853/3-1 of the German Science Foundation to V.S. Instruments were borrowed from the DEPAS pool. We acknowledge the efforts of the crews of RV *Polarstern* cruises ANT-XXIX/2+8 and ARK-XXIV/3, RV *Meteor* cruise M101 and RV *Marion Dufresne*.

Author Contributions V.S. planned and conducted the surveys, processed data for site 3 and wrote the paper. F.S. processed data from site 1. Both authors discussed the results and commented on the manuscript.

Author Information Reprints and permissions information is available at www.nature.com/reprints. The authors declare no competing financial interests. Readers are welcome to comment on the online version of the paper. Correspondence and requests for materials should be addressed to V.S. (Vera.Schindwein@awi.de).

Reviewer Information *Nature* thanks S. M. Carbotte and the other anonymous reviewer(s) for their contribution to the peer review of this work.

METHODS

Data processing. Seismic signals were identified with a short time average/long time average trigger in the continuous data stream of the OBSS, optimized for detecting all local earthquakes. All of the triggered events were reviewed by an analyst and spurious events were removed. P- and S-wave arrivals of all of the local earthquakes that were recorded by three or more stations were subsequently hand-picked and located with the linear least-squares algorithm Hyposat³², which also constrains the inversion with S-P travel-time differences.

One-dimensional velocity model. To derive a minimum one-dimensional velocity–depth profile, as commonly used in earthquake location³³, we used the results of refraction seismic surveys^{15,34,35} conducted within each of the study sites (Extended Data Figs 1a, 2a and 3a). We extracted smoothed average velocity–depth profiles for the upper 5 km, where the refraction seismic data provided sufficient ray cover. We thus constructed an initial velocity model and located all of the earthquakes. We used this preliminary location run to select a subset of well recorded events of at least 5 km depth that are situated within the network of stations. These events are considered the most sensitive to changes in the velocity model. We then tested a wide range of conceivable sub-Mohorovičić discontinuity (sub-Moho) velocities but kept the velocity model in the crust fixed as constrained by refraction seismic data. We located the subset of well constrained events for each velocity model and assessed the performance of each velocity model. We selected the velocity model that provided the lowest average root mean squared travel-time residual while still locating a large number of events. This final velocity model (Extended Data Figs 1b, 2b and 3b, red) was then used to locate all earthquakes.

Robustness tests. To assess the effects of the choice of velocity model on the location results and in particular to evaluate the reliability of the large hypocentre depths obtained, we performed several robustness tests. We located all of the events with a slow end-member velocity model with velocities reduced by 0.3 km s^{-1} compared with the final model and a fast end-member velocity model that consisted of a 4-km-thick crust underlain by velocities of 8 km s^{-1} , as is common for oceanic crust⁷ (Extended Data Figs 1b, 2b and 3b). Both low and high end-member velocity models produced a considerably poorer fit to the phase arrivals of all earthquakes as seen from the average root mean squared travel time residual in Extended Data Table 1. Fast sub-Moho velocities resulted in a failure to determine the hypocentre depth of many events at all three locations. The location algorithm had to fix the hypocentre depth to converge on the results. The number of well-determined hypocentre depths with depth errors of less than 5 km is therefore much smaller for the high-velocity model and illustrates its inappropriateness.

We further examined the effect of variations in the velocity model by $\pm 0.3 \text{ km s}^{-1}$ on hypocentre depth. The reduced velocity model is identical to the low-velocity end-member model tested above (Extended Data Figs 1b, 2b and 3b, orange). For the faster-velocity model we increased the velocities of the final velocity model by $+0.3 \text{ km s}^{-1}$ throughout but kept 8.0 km s^{-1} at 40 km depth fixed (Extended Data Figs 1b, 2b and 3b, purple) to avoid the convergence problems described above. Faster velocities again produced a poorer fit to the data and yielded fewer reliable hypocentre depths (Extended Data Table 2). These, however, are on average slightly shallower than hypocentres located with lower-velocity models. Changes in the average hypocentre depth are in all cases smaller than the average depth error and they are much smaller than the along-axis depth variations of the band of seismicity shown in Fig. 1 and interpreted here. Prominent deviations from the one-dimensional minimum velocity model due to local heterogeneities in the subsurface result in non-zero average station residuals rather than substantially shifting hypocentres. On site 3, the station located on the crest of the volcano showed a positive S-phase residual of on average 0.232 s. Omitting this station from the location procedure did not distort the pattern of hypocentres interpreted.

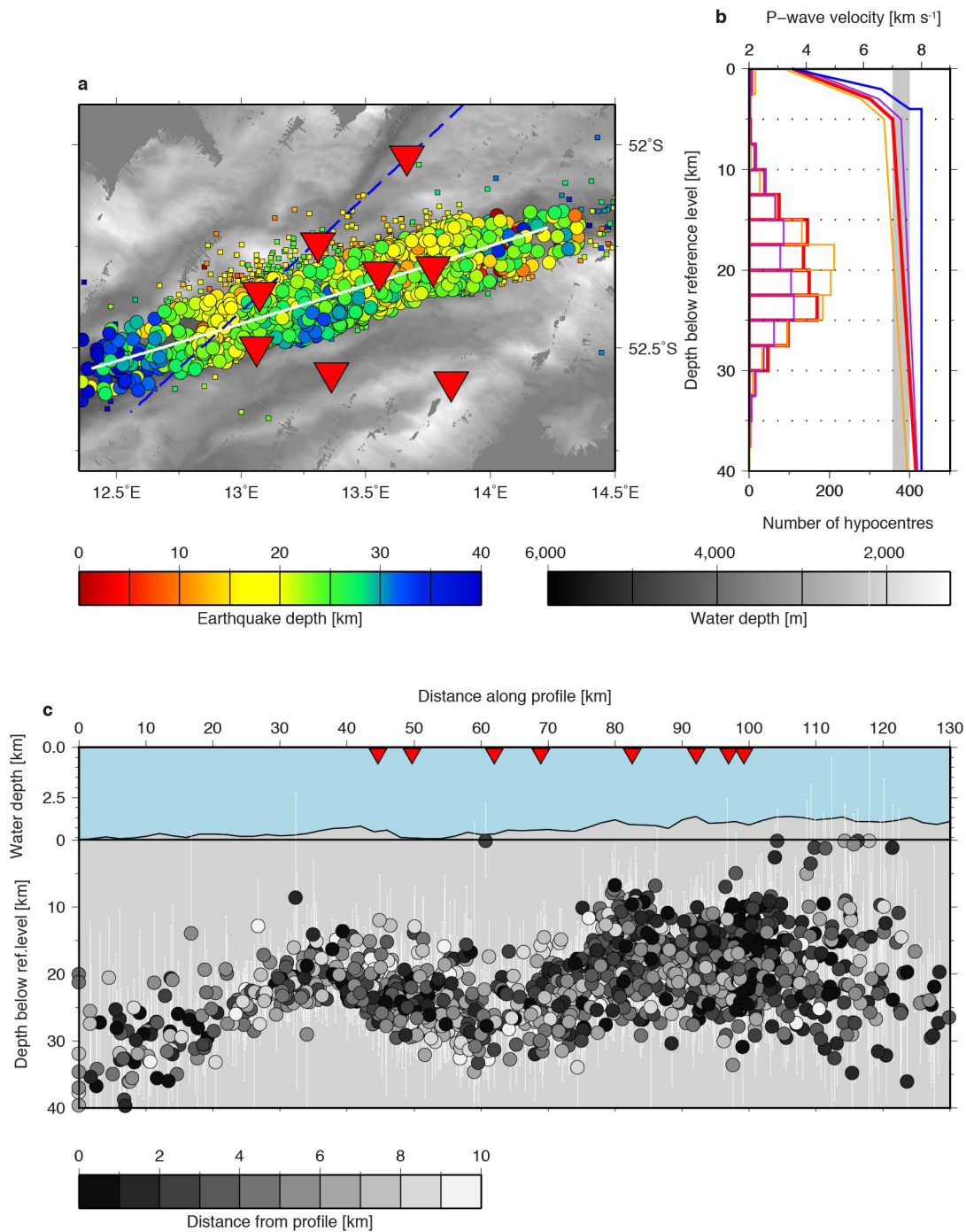
Selection and display of hypocentres. Extended Data Figs 1–3 show all 5,379 located earthquakes with a hypocentre solution, irrespective of location accuracy. These figures hence include also all smaller events. For Fig. 1 we imposed a maximum hypocentre depth error of 5 km as the sole quality criterion, fulfilled by 903, 441 and 2,625 events in data sets 1–3, respectively. The cross-sections displayed in Fig. 1 are based on a total of 3,664 events within 9.4 km of the cross-section profile. These events have a mean horizontal error of $\pm 3.5 \text{ km}$, a mean depth error of $\pm 2.7 \text{ km}$ and an average root mean squared travel-time residual of 0.24 s. Their locations were calculated from on average 15.5 phases at 6.3 stations, the closest station being on average 7.2 km away. For the majority of the events, the distance to the closest recording station is hence smaller than the hypocentre depth, which is generally considered necessary to obtain good hypocentre solutions. In Fig. 1, we highlight events outside the network where the distance to the next station becomes larger than the hypocentre depth. For these events, hypocentre depths have to be interpreted with care.

The band of seismicity was in all cases more or less flat-lying in the across-axis direction. Therefore, the projection of the hypocentres onto the cross-sections did not distort the seismicity pattern. Extended Data Figs 1c, 2c and 3c reveal no systematic dependence of hypocentre depth on projection distance. Aseismic regions interpreted here are furthermore not a consequence of earthquake selection as they appear in the full data set (Extended Data Figs 1–3) in the same way as in Fig. 1, indicating that these areas are also devoid of the weaker events that were omitted from Fig. 1.

Teleseismic events. Teleseismic earthquakes are used from a compilation⁵ of reviewed locations of the Bulletin of the International Seismological Centre occurring from 1976 to 2010 within 30 km of the rift axis for the Gakkal and Knipovich ridges and within 35 km of the rift axis for the SWIR owing to the larger location uncertainties there. A single-link cluster analysis identified earthquake clusters in time and space. Owing to their long observation period, teleseismic earthquake catalogues of mid-ocean ridges can reproduce the main features of along-axis seismicity variations on a regional scale that are visible in more complete catalogues of hydroacoustically recorded events²⁸. We project the event locations onto our profiles in Fig. 1 and count the number of teleseismic events in our 35-year-long catalogue in bins of 13 km, displayed as histograms in Fig. 1. We further calculate the average number of events per kilometre of the rift axis for comparison of the considered rift sections in Figs 1 and 2 and Extended Data Fig. 4. As the mean location uncertainty of the teleseismic events is about $\pm 31 \text{ km}$ for the SWIR compared with $\pm 12 \text{ km}$ at Gakkal Ridge⁵, we cannot unambiguously assign individual earthquakes to either amagmatic or magmatic subsections of the oblique supersegment, in particular. We therefore calculate seismicity rates for entire segments (Fig. 2 and Extended Data Fig. 4) or major portions thereof (Fig. 1) for comparison with adjacent segments. The average seismicity rates of the predominantly amagmatic supersegments contain some earthquakes that are connected with minor occurrences of magmatic lithosphere there. Purely amagmatic lithosphere may have even lower seismicity rates and the difference in the seismicity rate between amagmatic and magmatic lithosphere may be more pronounced.

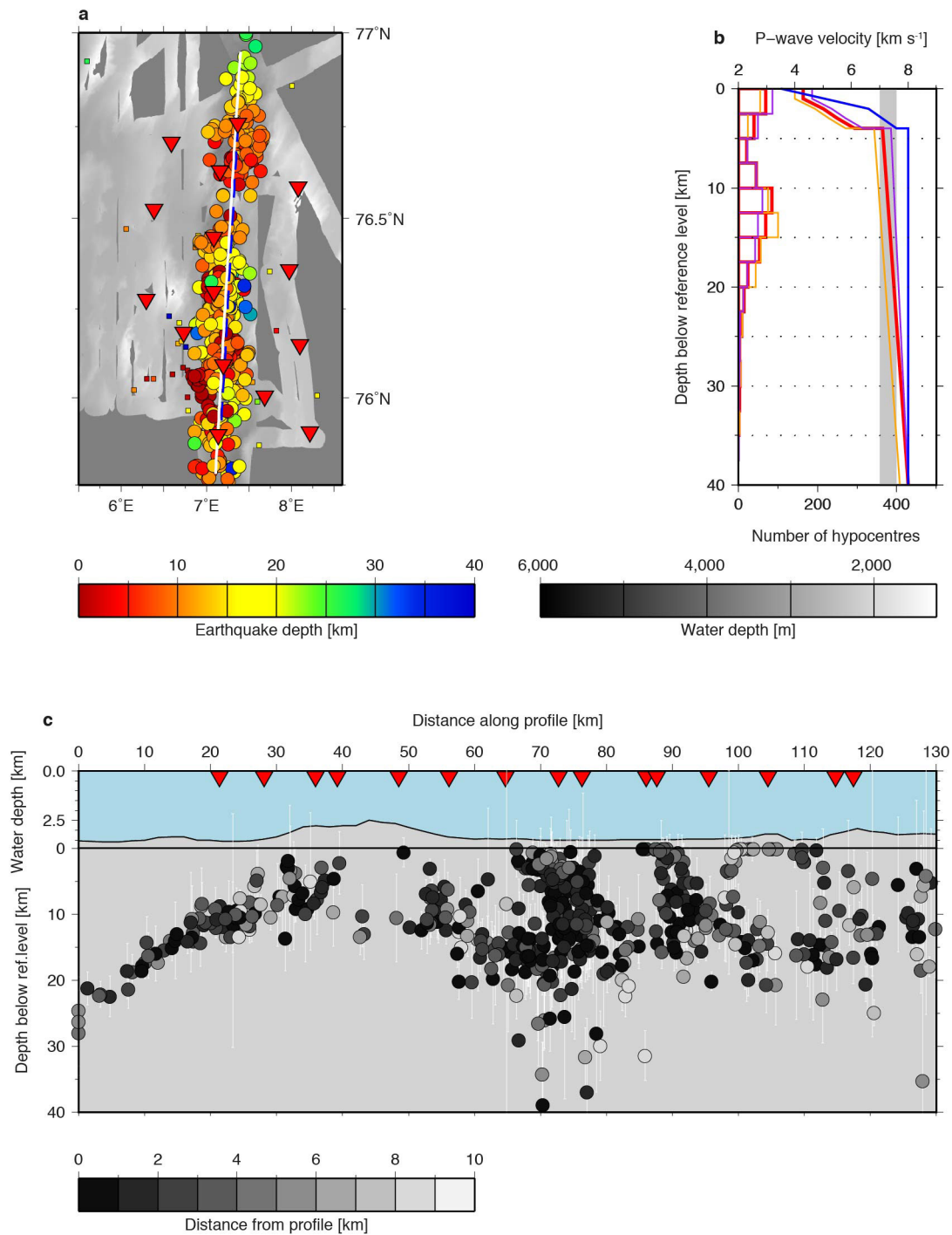
Figure 2 and Extended Data Fig. 4 show the individual teleseismic earthquake locations compared with a global map of magnetic anomalies³¹. Events that are part of clusters of two or more events occurring in close relation in time or space are highlighted. Note that such clusters occur only in regions of magmatic lithosphere. **Estimates of lithosphere temperature.** Absolute temperatures at the transition depth from brittle to ductile behaviour are discussed by several authors^{8,36,37} and their estimates range between $550 \text{ }^\circ\text{C}$ and $750 \text{ }^\circ\text{C}$. For mid-ocean-ridge lithosphere compositions, preference is given to higher temperatures within this range⁹. As mantle hotter than about $650 \text{ }^\circ\text{C}$ cannot build up long-term stresses, the base of seismicity and the transition between ductile and brittle rheologies have been associated with isotherms⁸. We therefore assume here that the maximum depth of seismicity delineates an isotherm of about $700 \text{ }^\circ\text{C}$. This value was chosen arbitrarily, the exact temperature is irrelevant for our conclusions. To obtain a crude estimate of the depth of the $400 \text{ }^\circ\text{C}$ isotherm in limited along-axis areas we assume a constant temperature gradient between the sea floor and the depth of the $700 \text{ }^\circ\text{C}$ isotherm. We furthermore assume that the $1,200 \text{ }^\circ\text{C}$ isotherm, used as a proxy for the lithosphere–asthenosphere boundary, has roughly the same along-axis topography as the $700 \text{ }^\circ\text{C}$ isotherm. Temperature fields calculated for mid-ocean-ridge axes^{26,38,39} show approximately constant spacing of isotherms in the brittle lithosphere and similar shapes of the $700 \text{ }^\circ\text{C}$ and $1,200 \text{ }^\circ\text{C}$ isotherms, justifying our assumptions.

32. Schweitzer, J. HYPOSAT—an enhanced routine to locate seismic events. *Pure Appl. Geophys.* **158**, 277–289 (2001).
33. Kissling, E., Ellsworth, W. L., Eberhart-Phillips, D. & Kradolfer, U. Initial reference models in local earthquake tomography. *J. Geophys. Res.* **99**, 19635–19646 (1994).
34. Jokat, W., Kollofrath, J., Geissler, W. H. & Jensen, L. Crustal thickness and earthquake distribution south of the Logachev Seamount, Knipovich Ridge. *Geophys. Res. Lett.* **39**, L08302 (2012).
35. Minshull, T. A., Muller, M. R. & White, R. S. Crustal structure of the Southwest Indian Ridge at 66°E : seismic constraints. *Geophys. J. Int.* **166**, 135–147 (2006).
36. McKenzie, D., Jackson, J. & Priestley, K. Thermal structure of oceanic and continental lithosphere. *Earth Planet. Sci. Lett.* **233**, 337–349 (2005).
37. Chen, W.-P. & Molnar, P. Focal depths of intracontinental and intraplate earthquakes and their implications for the thermal and mechanical properties of the lithosphere. *J. Geophys. Res.* **88**, 4183–4214 (1983).
38. Chen, W.-P. & Molnar, P. A nonlinear rheology model for mid-ocean ridge axis topography. *J. Geophys. Res.* **95**, 17583–17604 (1990).
39. Montési, L. G. J. & Behn, M. D. Mantle flow and melting underneath oblique and ultraslow mid-ocean ridges. *Geophys. Res. Lett.* **34**, L24307 (2007).



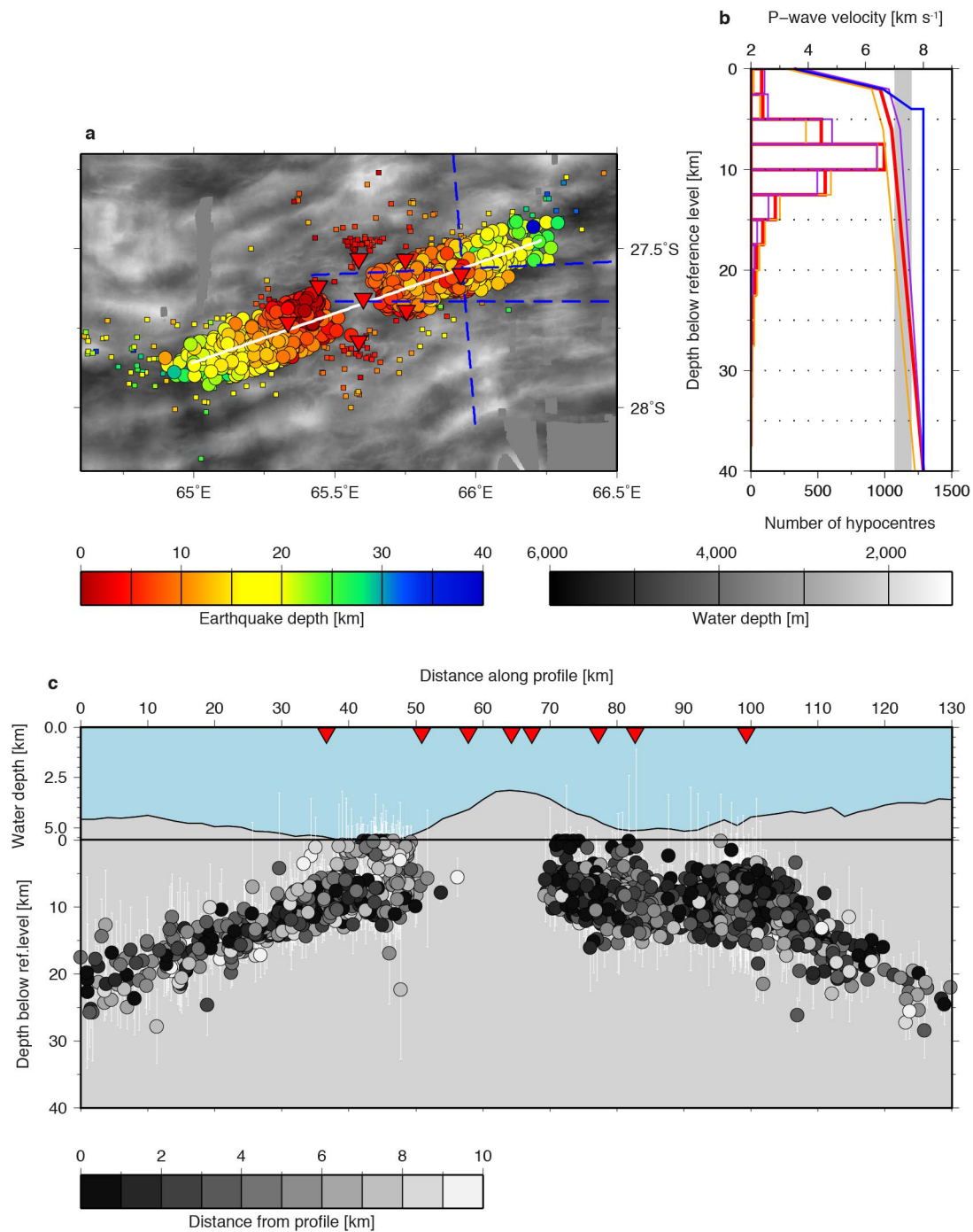
Extended Data Figure 1 | Earthquake location at survey site 1 including poorly located events. **a**, Epicentres (circles) colour-coded by hypocentre depth. Earthquakes not projected onto the cross-section (white line) in **c** are shown by squares. The red inverted triangles show OBS locations and the dashed blue line shows the position of the refraction seismic line¹⁵ used to constrain velocities in the uppermost lithosphere. **b**, The final velocity model used for earthquake location is shown in red, and the velocity models used for the robustness tests are shown in blue (the fast end-member representing a thin crust with ultramafic rocks underneath) orange (a velocity reduction of 0.3 km s^{-1} relative to the final model) and purple (a velocity increase of 0.3 km s^{-1} relative to the final model).

Velocities of $7.0\text{--}7.6 \text{ km s}^{-1}$ (grey bar) are considered anomalously low for lithospheric mantle. The histograms show the distribution of hypocentre depths obtained for the different velocity models. Faster models result in fewer well-located events, but the depth distribution is similar (see Extended Data Table 2). **c**, Cross-section of the hypocentres projected onto the axis and colour-coded according to the distance from the profile. The topography of the seismicity band is not an artefact of projection because at all depth intervals the earthquakes from various off-axis distances are present. The aseismic regions remain devoid of seismicity even when all poorly located earthquakes are shown.



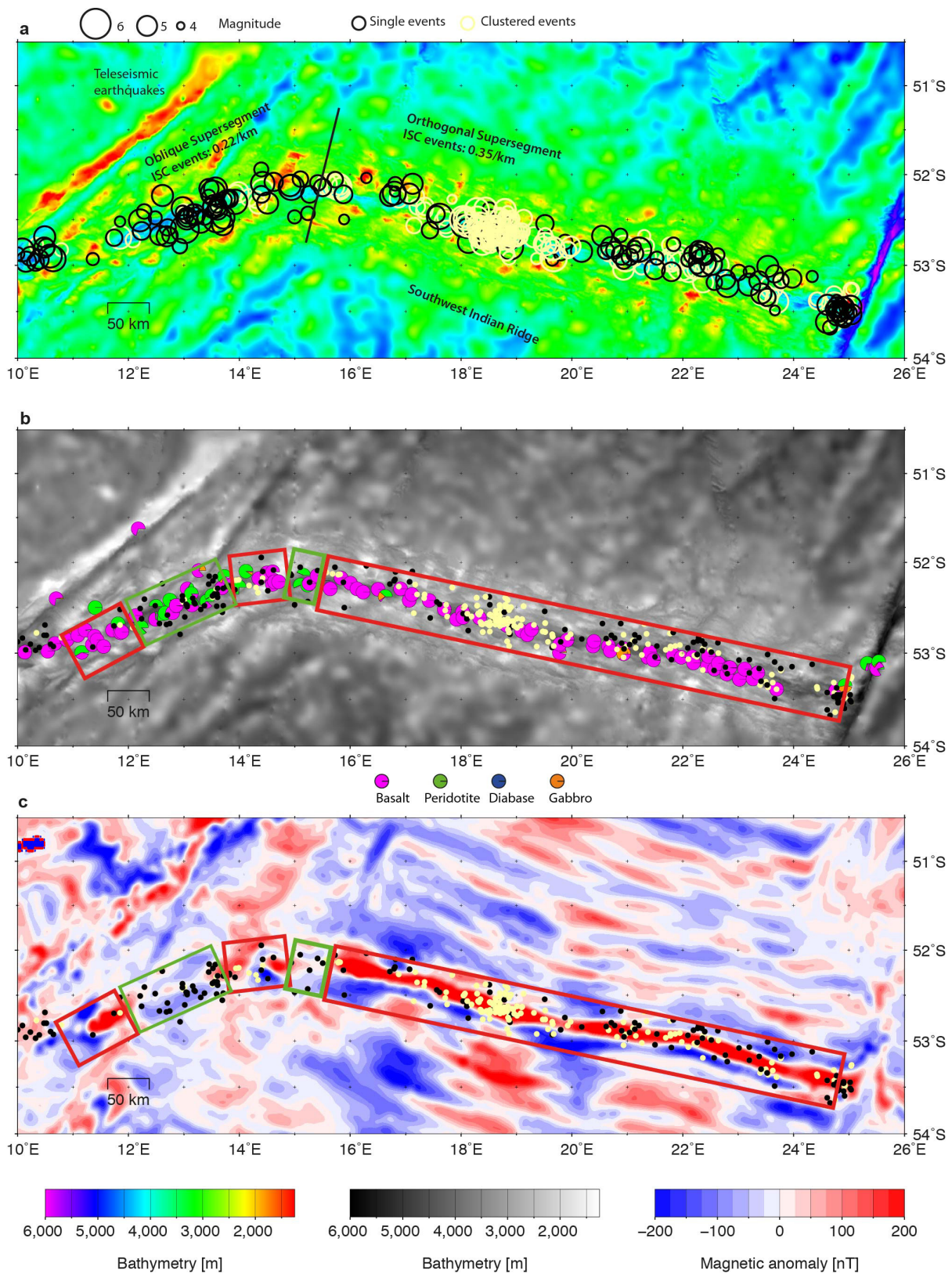
Extended Data Figure 2 | Earthquake location at survey site 2 including poorly located events. **a**, Epicentres (circles) colour-coded by hypocentre depth. Earthquakes not projected onto the cross-section (white line) in **c** are shown by the squares. The red inverted triangles show OBS locations and the dashed blue line indicates the position of the refraction seismic line³⁴ used to constrain velocities in the uppermost lithosphere. **b**, The final velocity model used for the earthquake location is shown in red and the velocity models used for the robustness tests are shown in blue (the fast end-member representing a thin crust with ultramafic rocks underneath) orange (a velocity reduction of 0.3 km s^{-1} relative to the final model) and purple (a velocity increase of 0.3 km s^{-1} relative to the final model).

Velocities of $7.0\text{--}7.6 \text{ km s}^{-1}$ (grey bar) are considered as anomalously low for lithospheric mantle. The histograms show the distribution of hypocentre depths obtained for the different velocity models. Faster models result in fewer well located events, but the depth distribution is similar (see Extended Data Table 2). **c**, Cross-section of the hypocentres projected onto the axis and colour-coded according to the distance from the profile. The topography of the seismicity band is not an artefact of projection because for all depth intervals the earthquakes from various off-axis distances are present. The aseismic regions remain devoid of seismicity even when all poorly located earthquakes are shown.



Extended Data Figure 3 | Earthquake location at survey site 3 including poorly located events. **a**, Epicentres (circles) colour-coded by hypocentre depth. Earthquakes not projected onto the cross-section (white line) in **c** are shown by the squares. The red inverted triangles show OBS locations and the dashed blue line indicates the position of the refraction seismic lines³⁵ used to constrain velocities in the uppermost lithosphere. **b**, The final velocity model used for the earthquake location is shown in red and the velocity models used for the robustness tests are shown in blue (the fast end-member representing a thin crust with ultramafic rocks underneath) orange (a velocity reduction of 0.3 km s^{-1} relative to the final model) and purple (a velocity increase of 0.3 km s^{-1} relative to the final model).

Velocities of $7.0\text{--}7.6 \text{ km s}^{-1}$ (grey bar) are considered as anomalously low for lithospheric mantle. The histograms show the distribution of hypocentre depths obtained for the different velocity models. Faster models result in fewer well-located events, but the depth distribution is similar (see Extended Data Table 2). **c**, Cross-section of the hypocentres projected onto the axis and colour-coded according to the distance from the profile. The topography of the seismicity band is not an artefact of projection because at all depth intervals the earthquakes from various off-axis distances are present. The aseismic regions remain devoid of seismicity even when all poorly located earthquakes are shown.



Extended Data Figure 4 | Contrasting magmatic and amagmatic sections of western SWIR. **a**, Teleseismic earthquake activity (open circles, scaled with magnitude) over bathymetry. The light yellow circles mark earthquake clusters of two or more events that are related in time and space. Data from ref. 5. **b**, Dredge lithology. Data from ref. 2. **c**, Magnetic anomalies. Data from ref. 31. Earthquakes from **a** are shown by the dots. The predominantly magmatic orthogonal supersegment shows

more abundant and often clustered teleseismic earthquakes and a marked magnetic anomaly. The predominantly amagmatic oblique supersegment shows less seismicity and peridotite exposure. Areas of magmatic and amagmatic lithosphere within this segment are defined from the seafloor lithology and magnetic patterns. The differences in the event rates within segments (see Fig. 2) are not visible here owing to a large uncertainty in earthquake locations.

Extended Data Table 1 | Location performance of the final one-dimensional velocity models and end-member models

Site Velocity model	Number of earthquakes located	Average rms residual [s]	Number of earthquakes with depth solution	Number of earthquakes with depth error < 5 km
Site 1				
Slow-end	1960	0.502	1896	990
Final	1959	0.485	1871	903
Fast-end	1959	0.546	1556	242
Site 2				
Slow-end	737	0.286	631	461
Final	736	0.264	614	441
Fast-end	744	0.364	441	181
Site 3				
Slow-end	2974	0.226	2880	2557
Final	2974	0.196	2894	2625
Fast-end	2970	0.235	1998	1555

The final velocity model of each site achieved the best fit to all of the observed phases. The high end-member velocity models produce fewer and unstable hypocentre depths.

Extended Data Table 2 | Dependence of the hypocentre depths on the velocity model

Site Velocity model	Number of earthquakes located	Number of earthquakes with depth error < 5 km	Average depth [km]	Average depth error [km]
Site 1				
- 0.3 km/s	1960	990	20.3	3.8
Final	1959	903	20.2	4.0
+ 0.3 km/s	1960	629	20.0	4.1
Site 2				
- 0.3 km/s	737	461	12.2	2.8
Final	736	441	10.9	2.6
+ 0.3 km/s	738	403	9.6	2.7
Site 3				
- 0.3 km/s	2974	2557	10.6	2.5
Final	2974	2625	9.5	2.3
+ 0.3 km/s	2970	2497	8.8	2.3

Only inverted hypocentre depths with a depth error of less than 5 km are included in the average values. The individual distributions are shown in Extended Data Figs 1b, 2b and 3b for each site. Note that the changes in average depth due to variations of the velocity model are in all cases smaller than the average depth error.